Handheld photoacoustic imaging of indocyanine green clearance for real-time quantitative evaluation of liver reserve function

Hai Zhang,[1,†] Si-Lue Zeng,[2,3,†] Yun-Zhu Wu,[1,3,4,†] Ruo-Xin Zhang,[5,†] Liang-Jian Liu,[3] Qiang Xue,[1,3] Jing-Qin Chen,[3] Kenneth K. Y. Wong,[6] Jin-Feng Xu,[1] Ya-Guang Ren,[3,7] Chi-Hua Fang,[2,8] and Cheng-Bo Liu[3,9]

[1]*Department of Ultrasound, Shenzhen People's Hospital, The Second Clinical College of Jinan University, The First Affiliated Hospital of Southern University of Science and Technology, Shenzhen 518020, China*
[2]*Department of Hepatobiliary Surgery I, Zhujiang Hospital, Southern Medical University, Guangzhou 510280, China*
[3]*Research Laboratory for Biomedical Optics and Molecular Imaging, CAS Key Laboratory of Health Informatics, Shenzhen Institute of Advanced Technology, Chinese Academy of Sciences, Shenzhen 518055, China*
[4]*Department of Ultrasound, West China Second University Hospital, Sichuan University, SiChuan 610044, China*
[5]*Shen Zhen Bay Laboratory, Guang Ming, ShenZhen,518000, China*
[6]*The University of Hong Kong, Department of Electrical and Electronic Engineering, Hong Kong, China*
[7]*yg.ren@siat.ac.cn*
[8]*fangchihua@smu.edu.cn*
[9]*cb.liu@siat.ac.cn*
[†]*Contributed equally*

Abstract: Preoperative assessment of liver function reserve (LFR) is essential for determining the extent of liver resection and predicting the prognosis of patients with liver disease. In this paper, we present a real-time, handheld photoacoustic imaging (PAI) system-based noninvasive approach for rapid LFR assessment. A linear-array ultrasound transducer was sealed in a housing filled with water; its front end was covered with a plastic wrap. This PAI system was first implemented on phantoms to confirm that the photoacoustic (PA) intensity of indocyanine green (ICG) in blood reflects the concentration of ICG in blood. *In vivo* studies on normal rabbits and rabbits with liver fibrosis were carried out by recording the dynamic PA signal of ICG in their jugular veins. By analyzing the PA intensity-time curve, a clear difference was identified in the pharmacokinetic behavior of ICG between the two groups. In normal rabbits, the mean ICG clearance rate obtained by PAI at 15 min after administration (PAI-R15) was below 21.6%, whereas in rabbits with liver fibrosis, PAI-R15 exceeded 62.0% because of poor liver metabolism. The effectiveness of the proposed method was further validated by the conventional ICG clearance test and pathological examination. Our findings suggest that PAI is a rapid, noninvasive, and convenient method for LFR assessment and has immense potential for assisting clinicians in diagnosing and managing patients with liver disease.

1. Introduction

Liver functional reserve (LFR) refers to the capacity of the liver to tolerate injuries caused by surgery, trauma, and liver diseases. It involves the liver's ability to repair and regenerate upon various injuries [1]. In clinical practice, LFR is a crucial assessment tool that can evaluate whether hepatic resection can be performed, the extent of resection, and the risk of hepatic failure after surgery for patients with benign and malignant liver tumors [2–4]. Accurate preoperative

evaluation of liver function is critical in patients undergoing hepatectomy to improve postoperative survival. In addition, LFR assessment helps assess the progression of liver lesions in patients with chronic liver diseases, such as cirrhosis and portal hypertension, determine optimal treatment options, and predict prognosis [5,6].

Several traditional static liver function tests, such as hematological tests [e.g., bilirubin, alkaline phosphatase (ALP)] and clinical grading systems (e.g., Child-Pugh class and the Model for End-stage Liver Disease) have been developed for predicting the extent of organic liver lesions [7,8]. Although they can identify the degree of organic lesions to a certain extent, they are not satisfactory in the comprehensive evaluation of LFR [9–11]. Moreover, their assessment accuracy can be affected by subjective variables, such as ascites status and degree of hepatic encephalopathy. Imaging modalities like computed tomography and magnetic resonance imaging allow for preoperative assessment of liver function and can help prevent postoperative liver failure; nevertheless, such protocols refer mainly to qualitative rather than quantitative assessment of LFR and cannot achieve real-time dynamic detection of LFR changes [12–14].

Dynamic tests, such as the indocyanine green (ICG) clearance test, are the most acknowledged method for LFR assessment. ICG, a water-soluble dye approved by the FDA, is selectively taken up by hepatocytes and excreted into the bile after intracellular transformation without any metabolic changes or extrahepatic ingestion. Thus, the rate of decline in the plasma concentration of ICG is closely correlated with liver function. This intrinsic hepatic clearance allows ICG to be widely used as a marker for LFR assessments. The gold standard for quantifying ICG clearance relies on *ex vivo* photometric analysis of consecutive blood samples obtained within 15 min of intravenous bolus injection; however, this process is invasive and inconvenient and cannot provide results in real time as it involves serial collection of venous blood (2 to 4 times). Pulse dye densitometry (PDD), which allows for percutaneous and noninvasive assessment, has been used as an alternative to this gold standard [15]. However, as this is not an imaging-guided measurement method, blood vessels cannot be intuitively visualized, and the random measurement position affects measurement accuracy, particularly in patients with poor peripheral blood circulation. Studies have shown a poor correlation between PDD and the gold standard spectrophotometry [16].

Therefore, a real-time, noninvasive, and convenient technique is warranted to achieve LFR assessment. Photoacoustic imaging (PAI) is a novel, noninvasive imaging modality that exploits different light absorption spectra of either endogenous chromophores, such as oxy- and deoxy-hemoglobin, or exogenous contrast agents, such as dye molecules [17,18]. PAI combines the high contrast of pure optical imaging with deep penetration of ultrasound (US) imaging, thus overcoming the effects of strong light scattering within biological tissues. PAI can generate images specific to the chromophore of interest [19,20]. Using illumination at specific wavelengths, the spatial distribution and concentration of individual absorbers in the animal bodies can be detected. In addition, parallel acoustic detection using a US transducer array with high repetition frequency allows real-time characterization of the signal intensity of the contrast agent in the target vessel. The above characteristics suggest that PAI can be an effective and convenient tool to monitor the *in vivo* pharmacokinetics and biodistribution [21]. Moreover, ICG is not only a metabolic dye for LFR assessment but also an excellent exogeneous contrast agent for PAI, with a strong photoacoustic (PA) signal at 805 nm in blood [22]. Previous studies have confirmed a good linear relationship between the PA signal of ICG and ICG concentration [23,24]. A study on hepatectomy disease model was presented to demonstrate the feasibility of using PAI to evaluate LFR by monitoring ICG pharmacokinetics [25]. In this study, we provide a new design of photoacoustic imaging technology which is user-friendly and convenient for hand-held operation. Furthermore, we established a new disease model and carried out quantitative analysis of ICG pharmacokinetics by analyzing multiple parameters.

In this study, we propose a real-time handheld PAI system for rapid LFR assessment. Phantom experiments were first conducted to confirm that the proposed method can be used to record the concentration of ICG in blood. In *in vivo* studies, normal rabbits and rabbits with liver fibrosis were used. By recording the dynamic PA signal of ICG in the jugular vein of rabbits, the ICG PA intensity-time curve was fitted, and the pharmacokinetic behavior of ICG was determined. According to both the phantom and *in vivo* experimental results, the proposed method can provide a new and convenient strategy for LFR assessment in clinical settings.

2. Materials and methods

2.1. Animal preparation and surgical procedure

All animal operations and procedures were approved by the Animal Ethics and Use Committee of the Shenzhen Institutes of Advanced Technology, Chinese Academy of Sciences. Adult male Japanese white rabbits (n = 10; 2.0–2.5 kg; 10 weeks old) were equally assigned to two groups. The normal group comprised five healthy rabbits, and the liver fibrosis group comprised five rabbits with bile duct ligation-induced liver fibrosis. The surgery began with anesthesia induction. The common bile duct was isolated at the duodenum approximately 3 cm from the pylorus of the stomach through a midline abdominal incision. A rigid plastic tube with a diameter of ~1.0 mm was used to ligate the bile duct, and the plastic tube was subsequently withdrawn to create a stenosis with a diameter of 1.0 mm in the hepatic ducts. After the procedure, hemostasis and sutures were performed, and antibiotic prophylaxis was administered. All animals were placed under the same living and feeding conditions (18°C−22°C, 12 h of light) and were fed a standard laboratory diet. All rabbits in the liver fibrosis group were confirmed as having developed liver fibrosis by histopathological analysis at the end of experiments.

2.2. Handheld PAI system

A custom-built, handheld, real-time PA and US dual-modality imaging system was used. As shown in Fig. 1, 805-nm nanosecond pulsed laser at a frequency of 20 Hz was transmitted to the sample surface through the optical fiber for stimulating the acoustic signal. The laser fluence at the sample surface was approximately 15 mJ/cm^2, which is well below the American National Standards Institute safety standard limit [26]. The generated US signal was received by a 128-element linear-array ultrasonic transducer, which was sealed in a housing with the optical fiber, as shown in the inset of Fig. 1. The front end of the housing was covered by plastic wrap with water inside so that the light and US signal can pass through. Then, the US signal was reconstructed using the back-projection algorithm to generate real-time PA images [27,28]. US images can provide structural information of blood vessels in real time and facilitate prompt adjustment of the imaging area. Rabbits were initially anesthetized with 3%−4% isoflurane in 100% oxygen. Anesthetized rabbits were placed on a regulated heating pad, and the body temperature was maintained at 37.5°C. The legs were fixed with strips of silk tape in slight abduction. The neck hair was shaved with an electric hair shaver, and the neck skin was smoothed using a depilatory cream. Spraying the neck skin of the rabbit with water and filling the space between the probe and the rabbit's neck skin with an US coupling gel can help obtain better coupling of PA signal propagation during imaging. The handheld dual-mode PA/US probe can also be fixed on a lifting platform to facilitate the fixation during the long imaging process.

2.3. Phantom test

Four samples were prepared separately to verify whether our PAI system could detect ICG signals and their changes in animal blood to promote further *in vivo* application of this system. Sample 1: 10 mL of blood was drawn through the central ear artery of a healthy rabbit weighing approximately 2.0 kg. Sample 2: 1 mL of ICG aqueous solution with a concentration of
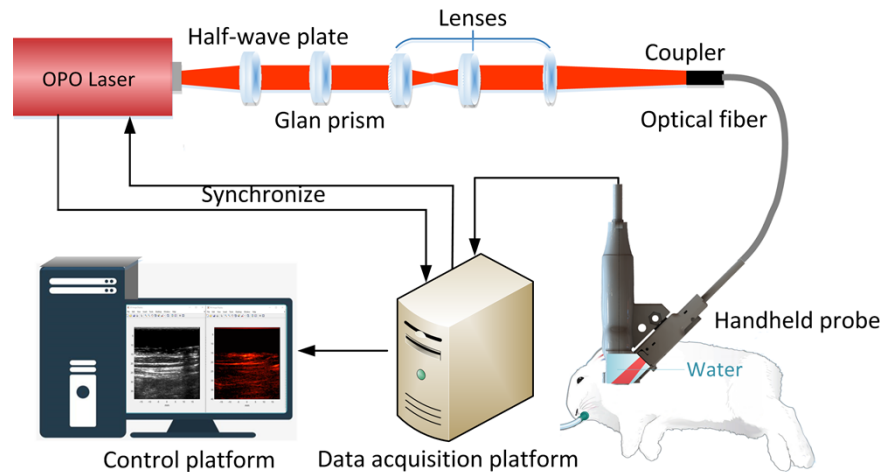
Fig. 1. Handheld PAI system used for real-time quantitative evaluation of LFR.

2.5 mg/mL was injected through the marginal ear vein in a rabbit, and 1 min after the injection, 2 mL of blood was collected from the rabbit's central ear artery. Sample 3: 1 mL of ICG aqueous solution was mixed with 9 mL of blood to obtain a mixture solution with a concentration of 0.25 mg/mL. Sample 4: 2.5 mg/mL of ICG aqueous solution was diluted to 0.25 mg/mL. Their PA signals were collected and analyzed.

Each sample above was injected into a sample tube and placed in the PAI system to obtain PA image data. The standard back-projection algorithm was used to reconstruct the PA images and the PA intensity of the region of interest was quantified to represent ICG in blood.

2.4. *In vivo blood ICG clearance study by handheld PAI*

Normal and liver fibrosis-diseased male Japanese white rabbits weighing 2.4–2.5 kg were used for the PA pharmacokinetics study. Rabbit jugular veins, along with the direction of blood flow, were identified as the imaging region for the blood clearance study using US imaging. The imaging probe was fixed above the imaging area. Using PAI, we continuously scanned the imaging region at a laser fluence of 15 mJ/cm^2 at 805 nm (the absorption peak of ICG in blood). The imaging was performed 5 min before ICG administration to establish a baseline signal. The ICG used in clinics was diluted into an aqueous solution (5 mg/mL). Then, the solution was injected through the rabbit marginal ear vein at a dose of 2.5 mg/kg. Subsequently, the handheld PA probe was fixed on a motorized positioning system for continuously monitoring the PA signal of the jugular vein region for 60 min. The PA intensity of ICG in the region of interest (ROI) was quantified to represent ICG metabolism by the liver.

2.5. *PAI analysis*

PA data obtained during the dynamic PAI study were analyzed by MATLAB (version 9.9, The Mathworks, Inc., Natick, MA, USA). The ROIs in each PA image were manually segmented according to the area of the jugular vein signal in each rabbit. The back-projection algorithm was applied to quantify the maximum projection intensity in the ROI before and after ICG administration at 11 different time points (before injection and 1, 5, 10, 15, 20, 25, 30, 40, 50, and 60 min after injection). The PA intensities of ICG (PAI$_{ICG}$) at these time points were obtained by subtracting the baseline signal before ICG injection from the signal after ICG injection for each rabbit. PA intensity RX (PAI-RX) of ICG was defined as ICG clearance in blood at *X* min and

calculated as the PA signal of ICG at X min normalized to the maximum value according to the following formula: $\text{PAI-RX} = \text{PAI}_{\text{ICG}(X)}/\text{PAI}_{\text{ICG (MAX)}}$.

The normalized PA intensity at X min (PAI-RX) was then interpolated with cubic splines to obtain the PA intensity-time curve of ICG before and after ICG injection. The half-life of ICG ($t_1/2$) refers to the duration it takes for the PA intensity to decrease to half of its peak value ($\text{PAI-RX}_{\text{(MAX)}}$) after injection. Meanwhile, the elimination time (T_0) is the duration required for the PA intensity to reach a steady-state after its initial decline.

To quantify the metabolism rate of ICG, an exponential model was used to analyze the decay of the normalized PA intensity after it reached the peak [25]:

$$\text{PAI - R}(X) = \text{PAI - RX}_{\text{(MAX)}} \cdot \exp(-k \cdot X) + c \tag{1}$$

The rate constant (k) indicates the decay constant of ICG. c is the constant offset of the curve.

2.6. Conventional ICG clearance test based on a draw of blood

Indwelling needles were first inserted into both the right marginal ear vein and the left central ear vein of the rabbit, respectively, to prepare for subsequent blood collection operations. Through the right marginal ear vein, a 2.5 mg/kg dose of ICG was intravenously injected, and through the left central ear vein, blood was collected before ICG injection and at 1-, 5-, 15-, and 60-min intervals after ICG injection. After each blood collection, the needle was sealed with normal saline and heparin sodium. Blood samples were then centrifuged at 3000 rpm for 20 min, and the supernate containing ICG was diluted 10× with sterile water. The absorbance of diluent solutions of serum was measured at 805 nm. The ICG absorbance ($\text{Absorb}_{\text{ICG}}$) at different time points was calculated by deleting the absorbance before ICG injection. ICG clearance rate in blood at X min measured by the conventional ICG clearance test method was calculated by normalizing the $\text{Absorb}_{\text{ICG}}$ to the maximum value according to the following formula: $\text{ICG-RX} = \text{Absorb}_{\text{ICG }(X)}/\text{Absorb}_{\text{ICG (MAX)}}$.

2.7. Statistical analysis

All data were presented as mean ± standard deviation. The graphs were prepared and statistical analysis was performed using the GraphPad Prism software (ver. 8.0, GraphPad Prism Software, Inc, La Jolla, CA, USA). Statistical comparisons between the normal and liver fibrosis groups were performed using an unpaired students' t-test. The correlation between the PAI-R15 and ICG-R15 was assessed using Pearson's correlative analysis. Statistical significance was defined at a P value of <0.05.

3. Results

3.1. PAI of phantom samples

Recording of PA signals and ICG concentrations in *in vitro* experiments was performed using the following samples: blood, aqueous ICG solution (0.25 mg/mL), ICG solution mixed with blood (0.25 mg/mL), and blood samples obtained after an intravenous ICG bolus injection (0.25 mg/mL). As shown in Fig. 2, PA images and intensity of these four samples were compared at 805 nm. Figure 2(a) shows that in the blood sample, only a weak signal was observed from the ROI, whereas a strong signal was present in the ROI for the aqueous ICG solution phantom. A stronger PA signal was observed in blood with injected ICG and blood mixed with ICG. Blood with injected ICG refers that the ICG aqueous was intravenously injected into a rabbit first, and then blood was collected through a vein of the rabbit after certain time. Blood mixed with ICG refers that blood was collected through a vein of the rabbit first, and then mixed with ICG aqueous solution *in vitro*. Quantitative analysis in Fig. 2(b) shows that the PA intensity of blood was the lowest (PA intensity = 25.739), whereas those of ICG aqueous solution, blood with injected

ICG and blood mixed with ICG were significantly higher (PA intensity = 99.104, 105.975 and 119.556 (a.u.), respectively).
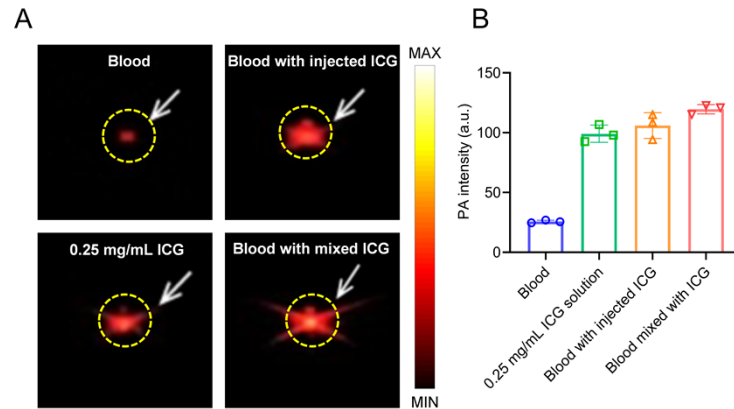

Fig. 2. *Ex vivo* PA analysis of blood and ICG. (a) PA images of blood, ICG aqueous solution, blood with injected ICG, and blood mixed with ICG (arrows point to the PA signal of the sample in phantom). (b) Quantitative PA analysis of the four samples.

The above results indicate that the PA intensity of blood was significantly improved with ICG addition, and the optical absorption properties of blood and ICG were not changed by the mixing of the two. The PA intensity of a mixture of ICG and blood is just the accumulation of the two. Therefore, the changes in PA intensity after ICG injection *in vivo* can reflect the changes in ICG concentration in blood after subtracting the baseline signal, i.e., the signal from blood contribution.

3.2. In vivo PAI and quantification

As shown in Fig. 1, the PA/US handheld probe was positioned directly above the rabbits' neck. Then, the jugular vein was monitored for 60 min. At each of the aforementioned time points, US and PA images were recorded simultaneously. The presented US images depict the physiological structure of a rabbit's neck with the skin layer visible on top (indicated by the red arrow). The anechoic tubular structure visible beneath the skin is identified as the jugular vein (indicated by the blue arrow). The green portions of the images are the reconstructed PA signals overlaid on the US image, which show varying intensities of PA signals. Representative time points (before injection and 1, 5, 15, and 60 min after injection) of the PA/US overlaid images of all the rabbits were selected as shown in Fig. 3. Figures 3(A) and 3(B) show the results of five rabbits in the normal and liver fibrosis groups, respectively. It can be seen that after the injection, the PA signal is significantly enhanced and subsequently declined with the metabolism of ICG in the liver until the end of the experiment (Visualization 1 in the Supplementary Materials displays the video for *in vivo* handheld PAI for real-time evaluation of LFR).

Quantitative analyses were also conducted, and the mean values of PAI-RX of different rabbits were calculated and cubic spline interpolation was used to obtain the PA intensity-time curve of ICG. Figures 3(C) and 3(D) show the PAI-RX, its mean value, and its interpolation curve for the five rabbits in the normal and the liver fibrosis groups, respectively. The curve of the normal group (Fig. 3(C)) rapidly reaches a steady-state that is only slightly higher than pre-injection level, indicating that the liver had almost entirely metabolized and eliminated ICG. According to this curve, we obtained the $t_1/2$ and T_0 of ICG, which is about 2.4 min. and 3.9 min., respectively. Then we employed the exponential decay model mentioned in section 2.5 to analyze the mean value of the normalized PA intensities in the normal group to simulate ICG metabolism. The rate
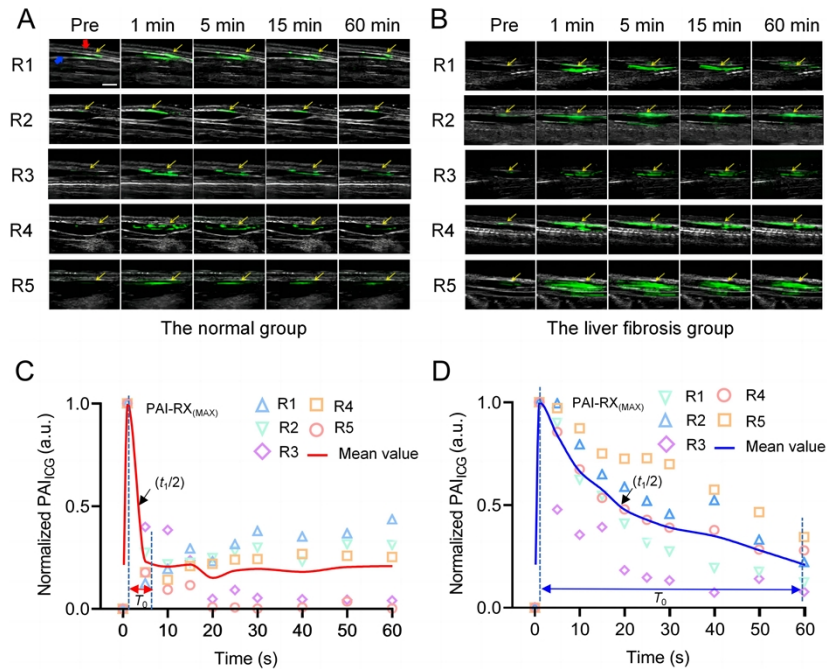
Fig. 3. *In vivo* PA (green) and US (gray) dual-modal imaging results of ICG metabolism. Distribution and excretion of ICG in the jugular vein of five rabbits in (A) the normal group and (B) the liver fibrosis group. Scale bar: 1 cm (C) Quantitative results of PA intensity shown in Fig. 3(A) and (D) quantitative results of PA intensity shown in Fig. 3(B) (the yellow arrow indicates the PA signal of the external jugular vein of the rabbit; the red arrow and blue arrow indicate the skin and jugular vein, respectively).

constant (k) of the normal group is found to be 0.76. In contrast, the PA intensity-time curve of ICG in the liver fibrosis group (Fig. 3(D)) do not exhibit a sharp decline as observed in the normal group. Instead, the intensity takes approximately 60 min. (T_0) to decrease to a level that is comparable to pre-injection, indicating an impaired function of hepatocytes which slow down the clearance rate of ICG. The $t_1/2$ of the liver fibrosis group is 17.5 min. and the rate constant (k) of the group is calculated to be 0.055.

3.3.   Conventional ICG clearance test results and correlation with PAI

Figures 4(A) and 4(B) illustrate the absorbance-time curves of ICG obtained by the conventional ICG clearance test based on ICG-RX and its mean values at different time points for five rabbits from the normal group and liver fibrosis group, respectively. The variation trend of these curves can reflect the metabolic process of ICG in blood, which is also consistent with the PA intensity-time curve of ICG (Figs. 3(C) and 3(D)).

According to the ICG metabolic results measured by both PAI (Fig. 3) and conventional ICG clearance test methods (Fig. 4), significant differences were seen between the normal group and liver fibrosis group, which were quantitatively analyzed and valued using an unpaired students' t-test method. According to the results shown in Figs. 5(A) and 5(B), ICG metabolism measured at 5 min and 15 min exhibited high correlation between both methods. However, results at 60 min were irrelevant, perhaps because ICG is almost completely metabolized at 60 min after the injection.
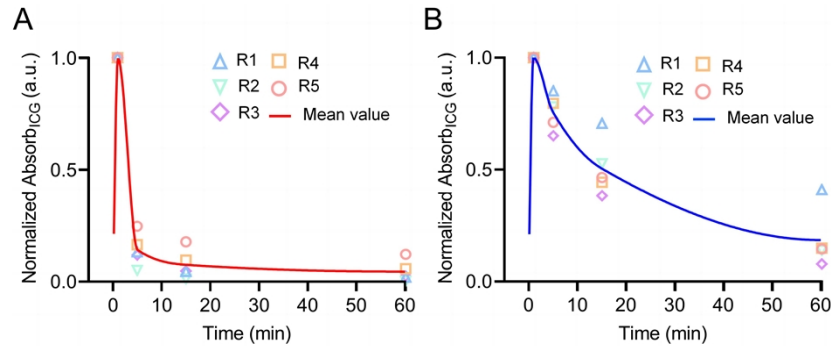
Fig. 4. ICG metabolic results obtained by the conventional ICG clearance test. Measurement results and the fitting curve of the mean value obtained by the classic ICG clearance test of five rabbits in (A) the normal group and (B) liver fibrosis group.
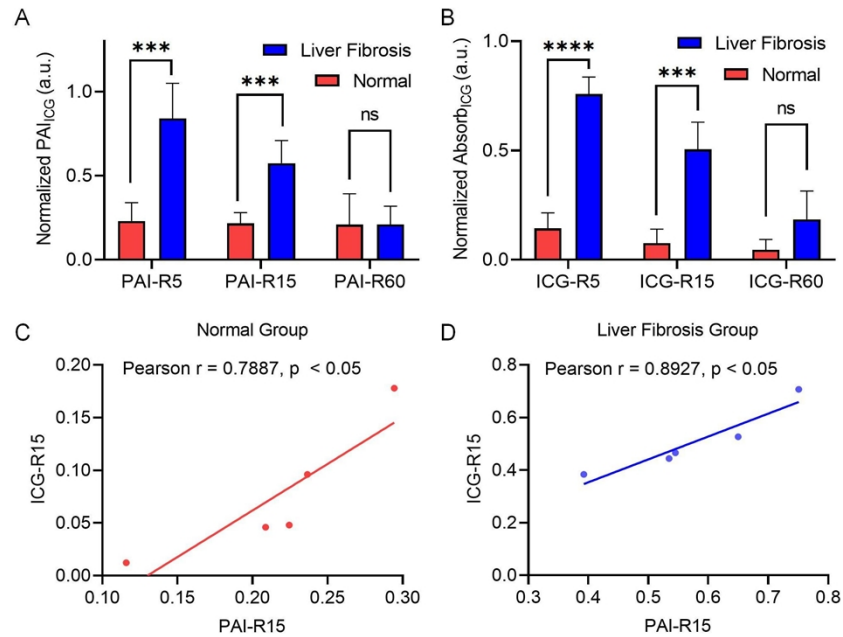

Fig. 5. Correlation analysis results between different groups and different methods. Correlation between the normal group and liver fibrosis group in terms of the ICG clearance rate at 5, 15, and 60 min using (A) PAI and (B) the conventional ICG clearance test method. Correlation between the PAI and the classic ICG clearance test method at 15 min in the (C) normal group and (D) liver fibrosis group. $*p < 0.05$, $**p < 001$, $***p < 0.001$, $****p < 0.0001$.

The most commonly used method of LFR assessment is the ICG clearance rate, which is measured 15 min after the injection. Therefore, to further validate the feasibility of using PAI to evaluate LFR, we calculated the ICG clearance rate at 15 min for the normal group and liver fibrosis group using PAI and classical ICG clearance test methods, respectively. Results are shown in Figs. 5(C) and 5(D). We found a significant correlation between PAI-R15 and ICG-R15 in both the normal group (Fig. 5(C), r = 0.7887, $P < 0.05$) and the liver fibrosis group (Fig. 5(D), r = 0.8927, $P < 0.05$).

3.4. Histopathological analysis of normal liver and liver fibrosis

To further validate the accuracy of PAI in assessing LFR, we performed anatomical and hematoxylin and eosin (H&E) staining analysis of rabbit livers in both groups. Figure 6(A) shows that the liver of the rabbit in the normal group is reddish brown with a soft texture and smooth surface, whereas Fig. 6(B) shows that the liver of the rabbit in the liver fibrosis group is greenish brown with a hard texture and tiny nodules on the surface. H&E staining of livers of five rabbits in the normal group showed that the morphology and structure of the lobules were normal and that there was no inflammatory cell infiltration in the portal area (Fig. 6(C)). Conversely, H&E staining of livers in the liver fibrosis group showed edema and necrosis of the interlobular bile duct epithelial cells with peripheral lymphocyte infiltration. The structure of the liver lobule was destroyed; the liver cord and lobule were disordered; and the interstitial fibrous tissue appeared proliferated. Pseudolobules were incompletely segmented by connective tissue around (Fig. 6(D)).
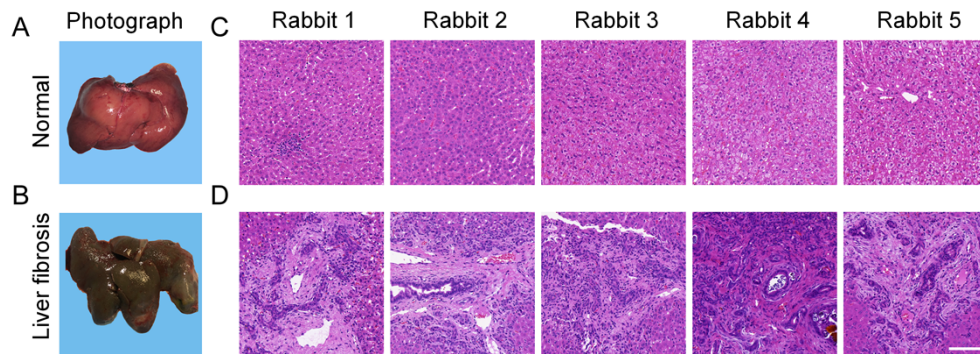

Fig. 6. Appearance and pathological results of the livers: (A) anatomical appearance of the liver in a normal rabbit. (B) Anatomical appearance of the liver of fibrotic rabbit. (C) Pathological images of five rabbits' liver in the normal group (H&E staining, × 20). (D) Liver pathological images of five rabbits in the liver fibrosis group (H&E staining, × 20). Scale bar: 100 μm.

4. Discussion

Assessment of LFR is essential to evaluate the indications for liver surgery and predict the progression and prognosis in patients with chronic liver diseases [29,30]. The ICG clearance test is the most acknowledged modality of assessing LFR. However, it is an invasive, time-consuming procedure that cannot acquire real-time information. Conversely, PAI is an emerging biomedical technique that avails the benefits of optical illumination and US detection. It combines the high contrast of optical imaging with high spatial resolution and superior penetration depth of US imaging. Moreover, because of the high laser pulse repetition rate, PAI can acquire real-time information about the *in vivo* distribution of the optical contrast agents, thus aiding quantitative analysis [31]. In this study, we proposed a dynamic continuous PAI system-based noninvasive

approach for rapid LFR assessment. We obtained the dynamic PA signal of ICG metabolism in rabbit jugular veins, plotted the PA intensity-time curve, and measured the pharmacokinetic behavior of ICG in rabbits. Taken together, a rapid, noninvasive and convenient LFR assessment was achieved, which presents a new strategy for clinical LFR assessment.

4.1.   Verification of phantom test

We first verified the feasibility of using PAI to detect ICG in blood using a phantom test. Previous research validated a linear relationship between the concentration of ICG and PA signal intensity [23,24]. In this study, ICG-containing blood and ICG diluent (0.25 mg/mL) were loaded in a phantom device using blood as the control reference, and the PA intensity signal was monitored using the custom-built PAI system. The relationship between the PA intensity signal and the ICG concentration supported that ICG in blood can be quantified by PAI. Therefore, it is suggested that changes in the PA intensity before and after ICG injection reflect the changes in ICG in blood.

4.2.   Discrimination ability of PAI

Based on the results of the in vitro phantom study, we further established a liver fibrosis model to verify the effectiveness of the imaging strategy on the LFR. Cholestatic liver fibrosis was induced in rabbits by bile duct ligation, which is a widely accepted classical experimental procedure. This protocol is simple with a good repetition rate, and the survival rates of the animals are high [32]. Bile duct ligation can induce a severe fibrotic response in the liver and cause a sharp decrease in the biliary excretion rate of ICG, thus resulting in the accumulation of ICG in the liver. Moreover, ICG will not regurgitate into the hepatic lymphatic vessels with bile duct obstruction [33]. Therefore, ICG concentration in peripheral blood is significantly lower in animal models with bile duct ligation-induced liver fibrosis than in animals with a healthy liver within a short time after ICG injection.

The jugular vein was selected as the ROI because it is relatively easy to be imaged clinically. Meanwhile, blood flow is slower in the veins than in the corresponding arteries, thus making ICG metabolism easier to monitor. The handheld integrated PAI system can rapidly locate the target area on the real-time image. By referring to the US images, the rabbit jugular vein was quickly located, and the angle of the probe was adjusted according to the real-time images. During the entire imaging process, the filling and elimination process of ICG in the jugular vein can be semi-quantitatively evaluated by observing the brightness changes in the PA image; this can be helpful for patients for whom rapid liver function assessment is required during liver surgery.

The PA images and PA intensity-time curve of the rabbit jugular veins at different time points before and after ICG administration can intuitively demonstrate ICG metabolism and the differences between the normal and liver fibrosis groups. Rabbits belonging to the normal group had healthy liver uptake and metabolism, and ICG in these animals was rapidly taken up and metabolized by the liver after intravenous injection. In these rabbits, the ICG concentration in the peripheral blood vessels sharply decreased, which is reflected in the PA intensity of the jugular vein. Conversely, rabbits in the liver fibrosis group showed severely impaired liver function, and in these rabbits, it took a long time for ICG to be cleared by the liver after ICG injection, thus allowing for the ICG concentration in peripheral blood vessels to persist at a relative high level compared to normal liver models after a long time following ICG injection.

4.3.   Correlation

Correlation analysis between the PAI method and the conventional ICG clearance test method was performed. The results showed a significant correlation, which indicated the feasibility of using the PA intensity collected from the jugular vein to reflect the ICG concentration *in vivo*.

ICG-R15 is widely used in clinical practice and is considered to be among the most valuable and reliable indicators for the assessment of LFR and prediction of post-hepatectomy liver failure in patients with liver fibrosis [34–36]. Thus, ICG-R15 was applied as the gold standard index in this study. Pearson correlation analysis was used to measure the correlation between PAI-R15 and ICG-R15 in the normal control and liver fibrosis groups. The results revealed the presence of a significant correlation, suggesting that the clearance rate calculated by PAI reflects the actual ICG metabolism in blood. These results suggest that PAI can become a clinical tool for LFR assessment after liver surgery and treatment.

5. Conclusion

In conclusion, this study presents a noninvasive and real-time method for LFR assessment based on a linear ultrasound transducer sealed in water-filled housing with an optical fiber. The compact and hand-held design of the device makes it suitable for clinical applications. We established a liver fibrosis model and obtained the clinical used parameter ICG-R15 using PAI, and then compared this parameter with the same parameter obtained with blood test. The results showed a significant correlation in both the normal group and the liver fibrosis group, suggesting that PAI method has the potential to be a reliable tool for assessing LFR. Furthermore, we selected the jugular vein of rabbits as the monitoring site, which would be convenient for clinical translation. However, to validate the stability of the method, larger population studies should be carried out. Additionally, further research is needed to investigate the accuracy of PAI in diagnosing and treating different types of liver diseases. Overall, this study provides a promising avenue to develop noninvasive and real-time method for assessing LFR.

Disclosures. The authors declare no conflicts of interest.

Data availability. All relevant data are available from the corresponding author upon request.

References

1. D. D'Avola, A. Granito, M. Torre-Aláez, and F. Piscaglia, "The importance of liver functional reserve in the non-surgical treatment of hepatocellular carcinoma," J. Hepatol. **76**(5), 1185–1198 (2022).
2. F. Manizate, S. P. Hiotis, D. Labow, S. Roayaie, and M. Schwartz, "Liver functional reserve estimation: state of the art and relevance for local treatments: the Western perspective," J Hepato Biliary Pancreat **17**(4), 385–388 (2010).
3. S. T. Fan, "Liver functional reserve estimation: state of the art and relevance for local treatments: the Eastern perspective," J Hepato Biliary Pancreat **17**(4), 380–384 (2010).
4. J. Lv, Y. Xu, L. Xu, and L. Nie, "Quantitative Functional Evaluation of Liver Fibrosis in Mice with Dynamic Contrast-enhanced Photoacoustic Imaging," Radiology **300**(1), 89–97 (2021).
5. P. D. Schneider, "Preoperative assessment of liver function," Surg. Clin. North Am. **84**(2), 355–373 (2004).
6. J. H. Yoon, J. I. Choi, Y. Y. Jeong, A. Schenk, L. Chen, H. Laue, S. Y. Kim, and J. M. Lee, "Pre-treatment estimation of future remnant liver function using gadoxetic acid MRI in patients with HCC," J. Hepatol. **65**(6), 1155–1162 (2016).
7. M. Malinchoc, P. S. Kamath, F. D. Gordon, C. J. Peine, J. Rank, and P. C. ter Borg, "A model to predict poor survival in patients undergoing transjugular intrahepatic portosystemic shunts," Hepatology **31**(4), 864–871 (2000).
8. D. J. Pinato, R. Sharma, and E. Allara, *et al.*, "The ALBI grade provides objective hepatic reserve estimation across each BCLC stage of hepatocellular carcinoma," J. Hepatol. **66**(2), 338–346 (2017).
9. A. Cucchetti, M. Cescon, F. Trevisani, and A. D. Pinna, "Current concepts in hepatic resection for hepatocellular carcinoma in cirrhotic patients," WJG **18**(44), 6398–6408 (2012).
10. Y. Y. Wang, X. H. Zhao, L. Ma, J. Z. Ye, F. X. Wu, J. Tang, X. M. You, B. D. Xiang, and L. Q. Li, "Comparison of the ability of Child-Pugh score, MELD score, and ICG-R15 to assess preoperative hepatic functional reserve in patients with hepatocellular carcinoma," J Surg Oncol **118**(3), 440–445 (2018).

11. E. El-Khateeb, A. S. Darwich, B. Achour, V. Athwal, and A. Rostami-Hodjegan, "Review article: time to revisit Child-Pugh score as the basis for predicting drug clearance in hepatic impairment," Aliment. Pharmacol. Ther. **54**(4), 388–401 (2021).

12. M. C. Lim, C. H. Tan, J. Cai, J. Zheng, and A. W. Kow, "CT volumetry of the liver: where does it stand in clinical practice?" Clin. Radiol. **69**(9), 887–895 (2014).

13. M. Huang, S. Shen, H. Cai, Z. Peng, W. Chiu, Z. P. Li, B. Peng, and S. T. Feng, "Regional liver function analysis with gadoxetic acid-enhanced MRI and virtual hepatectomy: prediction of postoperative short-term outcomes for HCC," Eur Radiol **31**(7), 4720–4730 (2021).

14. D. Geisel, L. Lüdemann, B. Hamm, and T. Denecke, "Imaging-based liver function tests–past, present and future," Fortschr Röntgenstr **187**(10), 863–871 (2015).

15. M. Reekers, M. J. Simon, F. Boer, R. A. Mooren, J. W. van Kleef, A. Dahan, and J. Vuyk, "Pulse dye densitometry and indocyanine green plasma disappearance in ASA physical status I-II patients," Anesth. Analg. **110**(2), 466–472 (2010).

16. T. Imai, K. Takahashi, F. Goto, and Y. Morishita, "Measurement of blood concentration of indocyanine green by pulse dye densitometry–comparison with the conventional spectrophotometric method," J Clin Monit Comput **14**(7/8), 477–484 (1998).

17. L. V. Wang and S. Hu, "Photoacoustic tomography: in vivo imaging from organelles to organs," Science **335**(6075), 1458–1462 (2012).

18. G. Huang, J. Lv, Y. He, J. Yang, L. Zeng, and L. Nie, "In vivo quantitative photoacoustic evaluation of the liver and kidney pathology in tyrosinemia," Photoacoustics **28**, 100410 (2022).

19. Q. Yu, S. Huang, Z. Wu, J. Zheng, X. Chen, and L. Nie, "Label-free visualization of early cancer hepatic micrometastasis and intraoperative image-guided surgery by photoacoustic imaging," J Nucl Med **61**(7), 1079–1085 (2020).

20. L. V. Wang and J. Yao, "A practical guide to photoacoustic tomography in the life sciences," Nat. Methods **13**(8), 627–638 (2016).

21. A. Attia, G. Balasundaram, M. Moothanchery, U. S. Dinish, R. Bi, V. Ntziachristos, and M. Olivo, "A review of clinical photoacoustic imaging: Current and future trends," Photoacoustics **16**, 100144 (2019).

22. P. Ott, "Hepatic elimination of indocyanine green with special reference to distribution kinetics and the influence of plasma protein binding," Pharmacol Toxicol **83**(Suppl 2), 1–48 (1998).

23. M. L. Landsman, G. Kwant, G. A. Mook, and W. G. Zijlstra, "Light-absorbing properties, stability, and spectral stabilization of indocyanine green," J Appl Physiol **40**(4), 575–583 (1976).

24. W. Song, Z. Tang, D. Zhang, N. Burton, W. Driessen, and X. Chen, "Comprehensive studies of pharmacokinetics and biodistribution of indocyanine green and liposomal indocyanine green by multispectral optoacoustic tomography," RSC Adv. **5**(5), 3807–3813 (2015).

25. T. Qiu, J. Yang, T. Pan, C. Peng, H. Jiang, and Y. Luo, "Assessment of liver function reserve by photoacoustic tomography: a feasibility study," Biomed. Opt. Express **11**(7), 3985 (2020).

26. L. I. O. America, "ANSI Z136.1: American National Standard for Safe Use of Lasers," (2007).

27. M. Xu and L. V. Wang, "Universal back-projection algorithm for photoacoustic computed tomography," Phys. Rev. E **71**(1), 016706 (2005).

28. P. Burgholzer, T. Berer, H. Gruen, H. Roitner, J. Bauermarschallinger, R. Nuster, and G. Paltauf, "Photoacoustic tomography using integrating line detectors," J. Phys.: Conf. Ser. **214**(1), 012009 (2010).

29. M. N. Thomas, E. Weninger, M. Angele, F. Bösch, S. Pratschke, J. Andrassy, M. Rentsch, M. Stangl, W. Hartwig, J. Werner, and M. Guba, "Intraoperative simulation of remnant liver function during anatomic liver resection with indocyanine green clearance (LiMON) measurements," HPB **17**(6), 471–476 (2015).

30. C. Huang, Z. Chen, T. Wang, X. He, M. Chen, and W. Ju, "A marginal liver graft with hyperbilirubinemia transplanted successfully by ischemia-free liver transplantation," Ann Transl Med **9**(5), 425 (2021).

31. Y. Li, L. Li, L. Zhu, K. Maslov, J. Shi, P. Hu, E. Bo, J. Yao, J. Liang, L. Wang, and L. V. Wang, "Snapshot Photoacoustic Topography Through an Ergodic Relay for High-throughput Imaging of Optical Absorption," Nat. Photonics **14**(3), 164–170 (2020).

32. C. Liedtke, T. Luedde, T. Sauerbruch, D. Scholten, K. Streetz, F. Tacke, R. Tolba, C. Trautwein, J. Trebicka, and R. Weiskirchen, "Experimental liver fibrosis research: update on animal models, legal issues and translational aspects," Fibrog. Tissue Repair **6**(1), 19 (2013).

33. T. Kimura, S. Nakayama, T. Yamao, Y. Kurosaki, and T. Nakayama, "Pharmacokinetics of indocyanine green in rats with experimentally induced hepatic diseases," Biol Pharm Bull **16**(11), 1140–1145 (1993).

34. T. Matsumata, T. Kanematsu, Y. Yoshida, T. Furuta, K. Yanaga, and K. Sugimachi, "The indocyanine green test enables prediction of postoperative complications after hepatic resection," World J. Surg. **11**(5), 678–681 (1987).

35. H. Imamura, K. Sano, Y. Sugawara, N. Kokudo, and M. Makuuchi, "Assessment of hepatic reserve for indication of hepatic resection: decision tree incorporating indocyanine green test," J Hepatobiliary Pancreat Surg **12**(1), 16–22 (2005).

36. Y. Watanabe and K. Kumon, "Assessment by pulse dye-densitometry indocyanine green (ICG) clearance test of hepatic function of patients before cardiac surgery: its value as a predictor of serious postoperative liver dysfunction," J. Cardiothorac. Vasc. Anesth. **13**(3), 299–303 (1999).